

1 **Quantitative visualization of two-phase flow in a**
2 **fractured porous medium**

3 **Zhen Liao^{1,2}, Russell L. Detwiler³, Esther Cookson³, Wanjun Lei^{1,2}, Yi-Feng**
4 **Chen^{1,2}**

5 ¹State Key Laboratory of Water Resources Engineering and Management, Wuhan University, Wuhan
6 430072, China

7 ²Key Laboratory of Rock Mechanics in Hydraulic Structural Engineering of the Ministry of Education,
8 Wuhan University, Wuhan 430072, China

9 ³Department of Civil and Environmental Engineering, University of California Irvine, Irvine, CA, United
10 States

11 **Key Points:**

- 12 • Developed a novel experimental method to visualize two-phase flow in a fracture
13 in a porous matrix.
- 14 • The evolution of the air-water distribution within the fracture was measured dur-
15 ing sequential drainage and imbibition experiments.
- 16 • Capillary head versus saturation curves are sensitive to the pore-size distribution
17 of the bounding porous matrix.

Corresponding author: Russell L. Detwiler, detwiler@uci.edu

Abstract

Two-phase fluid flow in fractured porous media impacts many natural and industrial processes but our understanding of flow dynamics in these systems is constrained by difficulties measuring the flow in the interacting fracture and porous media. We present a novel experimental system that allows quantitative visualization of the air and water phases in a single analog fractured porous medium. The fracture system consists of a sintered-glass porous plate in contact with an impermeable glass plate. A reservoir connected to the porous plate allows control of pore pressure within the porous medium. The fracture fills and drains through the porous matrix and flow manifolds along two edges of the fracture. The fracture is mounted in an imaging system that includes a controlled light-emitting diode (LED) panel and a charge-coupled-device (CCD) camera. Flow and pressure are controlled and monitored by a computer during experiments. To demonstrate this system, we carried out a series of cyclic drainage and imbibition experiments in fractures bounded by porous media with different pore-size distributions in the porous matrix. Images of the drainage process demonstrate that the air-water distribution within the fracture evolves differently than has been observed in non-porous fractured systems. Specifically, we observed limited trapping of water within the fracture during drainage. Conversely, during imbibition, because air cannot exit through the porous matrix, significant regions of air became entrapped once pathways to the fracture boundaries became water filled. The differences in phase evolution led to substantial differences in the evolution of estimated relative permeability with saturation.

1 Introduction

Two-phase flow in fractured porous media plays an important role in natural processes such as infiltration into fractured rock and engineered processes such as enhanced oil/gas recovery (Karpyn et al., 2009; Rangel-German & Kovscek, 2002), geological CO₂ sequestration (Vafaie et al., 2023), and remediation of groundwater contaminated by non-aqueous phase liquids (NAPL) (Dearden et al., 2013). Related two-phase flow processes can be broadly categorized as either drainage (non-wetting phase displaces the wetting phase) or imbibition (wetting phase displaces the non-wetting phase).

Early studies of two-phase flow through fractures considered fractures in a non-porous matrix. These studies included experiments in transparent models (e.g., Nicholl et al.,

1994; Su et al., 1999) or replicas (e.g., Persoff & Pruess, 1995; Wan et al., 2000) and invasion percolation simulations in variable aperture fields (e.g., Glass et al., 1998; Xu et al., 1998; Yang et al., 2012). In such fractures, flow of the two fluids occurs only through the fracture and the distribution of the phases depends on characteristics of the fracture aperture and the nature and history of the displacement processes. Furthermore, both the wetting and non-wetting fluid may become entrapped and immobilized in regions that are isolated from the fracture boundaries.

When the fractured matrix contains non-negligible porosity, flow of one or both fluids can occur through the fracture and the porous matrix. Two general experimental approaches have been used to study two-phase flow in fractured porous media. The first approach uses micromodels that represent a two-dimensional (2D) cross-section through a fracture; the fracture is a 2D channel and the adjacent porous matrix is a 2D slice of porous medium (e.g., Haghighi et al., 1994; Wan et al., 1996; Rangel-German & Kovscek, 2006). Such experimental systems allow direct visualization of the interaction of multiple phases within the fracture and porous matrix, but neglect the 3D interaction of the phases within the fracture induced by aperture variability.

The second approach combines two-phase flow through cores of fractured porous rock with X-ray computed tomography to observe the distribution of phases within the fracture and porous matrix (Rangel-German & Kovscek, 2002; Karpyn et al., 2009; Arshadi et al., 2018). This has the advantage of providing measurements of the distribution of two or more phases within the pore space (both fracture and porous matrix) in fractured cores. However, the temporal and spatial resolution of CT scans constrains the scalability of these studies. For example, Arshadi et al. (2018) imaged 5-mm segments of a larger fractured core at a $2.5\text{-}\mu\text{m}$ voxel resolution. Such high spatial resolution facilitates identification of phases within pores in the matrix, but limits the size of the fracture that can be imaged.

We developed a novel fractured porous media experimental test cell that consists of a translucent porous glass surface mated with a transparent non-porous glass surface. Quantitative visualization techniques facilitate direct measurement of the evolving phase distribution within the $15\times 15\text{-cm}$ fracture at a spatial resolution of $\sim 75\ \mu\text{m}$ and a temporal resolution of $\sim 1\ \text{Hz}$. We demonstrate the new system through a series of drainage and imbibition experiments in fractures with two different pore-size distributions in

81 the porous matrix. We details the experimental system and fabrication of the fracture
82 model in Section 2 ; Section 3 describes the experimental procedure used to demonstrate
83 the results along with the required data analyses; Section 4 presents the results of the
84 demonstration experiments; and Section 5 provides concluding remarks.

85 2 Experimental System

86 The experimental system (Figure 1a) includes a test stand that rigidly supports
87 a 12-bit CCD camera (Quantix KAF-6303e; 2048×3072 pixels), red LED backlight panel
88 (with an emitted wavelength of ~ 625 nm) and the experimental model. The test stand
89 can rotate from -90° to 90° so gravitational forces acting on the fluid in the fracture
90 can be varied. The spatial resolution of images of the fracture plane was $75 \times 75 \mu\text{m}$.
91 Opaque fabric covers the test stand to minimize stray light in the imaging system. Sim-
92 ilar experimental systems have been used to study a range of flow and transport processes
93 in single variable aperture fractures (e.g., Nicholl et al., 1999; Detwiler et al., 1999, 2002)

94 [Figure 1 about here.]

95 In this study, we have developed a novel fracture test cell that includes a porous
96 fracture surface. Figure 1b shows a schematic of the fractured porous medium test cell.
97 A porous glass plate (bottom) mated with a smooth glass plate (top) served as the 15×15 -
98 cm fracture surfaces. A unique feature of this configuration is that the bottom porous
99 surface is both permeable and translucent, so transmitted light can be measured dur-
100 ing experiments. Thus, changes in measured transmitted light intensity reflect the evol-
101 ving distribution of air and water within the fracture (see Section 3.2 for details). Fur-
102 thermore, using porous glass with different pore sizes provides the opportunity to directly
103 quantify the influence of matrix porosity and permeability on two-phase flow processes
104 in fractured porous media. The example experiments presented here used two different
105 pieces of porous glass surfaces (Rudong Shundao Glass Instrument Factory, China) with
106 reported pore-size distributions of $4\text{-}7 \mu\text{m}$ (FF - fracture with fine pore-size matrix) and
107 $16\text{-}30 \mu\text{m}$ (MF - fracture with medium pore-size matrix).

108 Two 1.9-cm-thick fused-quartz windows supported by aluminum frames enclosed
109 the fracture surfaces. Clear polyvinyl chloride (PVC) gaskets separated each fracture sur-
110 face from the fused-quartz window creating empty cavities between each fracture sur-

111 face and the supporting window. A needle through the gasket into the lower cavity pro-
 112 vided an inlet/outlet for water flow in/out of the porous matrix. To prevent leakage from
 113 the edges of the porous lower surface, a rim of dyed epoxy was applied along the periph-
 114 eral edges of the porous glass (see Text S1, Figure S1 and Figure S2 for additional de-
 115 tails).

116 After placing the smooth glass and the porous glass surfaces in contact to create
 117 the fracture, normal stress was applied to the frame by tightening the connecting bolts
 118 to a uniform torque (typically 1.7 N·m). Figure 1b shows a rigid frame surrounding the
 119 fracture with bolts that apply force to the no-flow boundaries (left and right sides) and
 120 flow manifolds (top and bottom). The flow manifold has a $\sim 3 \times 5$ -mm channel along
 121 the entire width of the fracture to ensure that pressure gradients along the manifold chan-
 122 nel are negligible relative to pressure gradients within the fracture.

123 Fluid entered and exited the fracture through tubing connected to the cavity nee-
 124 dle and the flow manifolds. For the experiments presented here, a Marriotte bottle con-
 125 nected to the cavity needle served to control the head in the permeable matrix (bottom
 126 fracture surface). The Marriotte bottle was positioned on an analytical balance (Met-
 127 tler Toledo MS4002S/03) on a variable-height stage, which allowed reproducible head
 128 changes of up to ± 70 cm relative to the middle of the fracture plane. We define the cap-
 129 illary head as:

$$\Psi = \frac{p_a - p_w}{\rho_w g} = \frac{p_c}{\rho_w g} \quad (1)$$

130 where p_a , p_w , and p_c are the atmospheric, water, and capillary pressure, respectively, ρ_w
 131 is the density of water and g is acceleration due to gravity. During all experiments, a pres-
 132 sure transducer (Validyne DP15-42) monitored p_w at 0.167 Hz. Mass flow rate in and
 133 out of the fracture was recorded by the analytical balance. A computer connected to the
 134 experimental system controlled data acquisition from each of the sensors (camera, pres-
 135 sure transducer, and balance) using Labview (e.g., Bitter et al., 2006). Manometers ad-
 136 jacent to the pressure transducer facilitated periodic calibration of the pressure trans-
 137 ducer but were isolated from the fracture during drainage and imbibition experiments.
 138 Because Marriotte bottles lead to small pressure oscillations when bubbles release from
 139 the vent tube, we terminated the vent tube with a 16-gauge needle and applied a 0.4 atm
 140 vacuum to the head space in the bottle. This caused a steady stream of bubbles from

141 the vent tube and negligible pressure oscillations. To minimize evaporation losses from
142 the Marriotte bottle, we humidified the vent air entering the bottle (Figure 1).

143 **3 Cyclic Drainage and Imbibition Experiments**

144 To demonstrate the capabilities of this new experimental system, we carried out
145 several cyclic drainage and imbibition experiments. Horizontal experiments were carried
146 out in the MF and FF models (Experiments MFH and FFH, respectively) to investigate
147 the effect of the matrix permeability, and one vertical experiment was conducted in FF
148 model (Experiment FFV) to explore the added effect of gravity. Note, results from MFH
149 and FFH are discussed in Section 4; the results of FFV are included in the Supplemen-
150 tary Information (Text SS5).

151 **3.1 Experimental Procedure**

152 Each experimental sequence involved: primary drainage \rightarrow primary imbibition \rightarrow
153 secondary drainage \rightarrow secondary imbibition. Before each experiment, carbon dioxide was
154 injected through the cavity, porous matrix and dry fracture to displace air from the test
155 cell. Then deionized, de-aired water was injected to saturate the fracture. Prior to ini-
156 tializing the first drainage sequence, the boundary conditions for the fracture were es-
157 tablished. For the horizontal experiments, the flow manifolds and all connected tubing
158 were drained so the manifolds were filled with air at atmospheric pressure. For the ver-
159 tical experiment, the top flow manifold and connected tubing were drained, establish-
160 ing a zero-pressure, air boundary at the top of the fracture, while the bottom manifold
161 and connected tubing were valved off, establishing a no-flow boundary at the bottom of
162 the fracture.

163 The drainage-imbibition cycles were conducted by sequentially varying the capil-
164 lary head in the cavity through a set of static displacements of the Marriotte bottle. Im-
165 age acquisition began before initially changing the position of the Marriotte bottle and
166 continued until the final drainage or imbibition step. During each step, the valve be-
167 tween the cavity and Marriotte bottle (E) was closed as the height of the bottle was ad-
168 justed. The valve was then opened and the fracture was allowed to drain or fill until equi-
169 librium. We determined when equilibrium was reached by observing differences between
170 successive raw images and differences between successive mass readings from the digi-

171 tal balance recording the mass of the Mariotte bottle. Each drainage-imbibition cycle
172 was completed during a single day followed by an approximately 12-hour pause before
173 completing the secondary drainage-imbibition cycle.

174 **3.2 Measurement of Evolving Phase Distribution**

175 To aid interpretation of the images acquired during experiments, we developed an
176 image processing script in MATLAB to convert raw images to binary images that dis-
177 tinguished the two phases (air / water). Figure 2 shows the steps of the image process-
178 ing procedure. At the start of each experiment, we took a sequence of 100 reference im-
179 ages of the saturated matrix and fracture, which we averaged to yield a single, low-noise
180 reference image (Figure 2a). To account for nonuniformities in light transmission through
181 the porous matrix and fracture, we normalized each experimental image (Figure 2b) by
182 the reference image. The natural logarithm of the resulting normalized field quantifies
183 light absorbance at each pixel (Figure 2c).

184 [Figure 2 about here.]

185 Light scattering at the interface between the porous matrix and the fracture com-
186 plicates differentiating air and water within the fracture. Rather than a sharp edge, the
187 air-water interface appears in the absorbance field as a diffuse zone where the values tran-
188 sition from near zero for water to approximately 0.2 for air (Figure 2c). To quantify the
189 location of the interface, we sought a global threshold that minimized the number of air
190 clusters during the primary drainage cycle. The rationale for this approach is that, dur-
191 ing primary drainage, we expect the formation of a connected air cluster originating from
192 the fracture inlet with minimal fragmenting of this cluster until the beginning of the sub-
193 sequent imbibition cycle. Due to noise in the images, smaller threshold values cause lo-
194 calized water-filled regions to be misidentified as air resulting in an increase in the num-
195 ber of air-filled clusters. Larger threshold values cause some thin air-filled channels to
196 be misidentified, separating the large invading cluster into multiple clusters.

197 To determine the global absorbance threshold, we developed an algorithm that se-
198 quentially incremented the threshold over a range that included the likely global thresh-
199 old value, binarized the field according to each threshold value and counted the result-
200 ing number of discrete air clusters. We repeated this process for each image during the

201 primary drainage cycle. Plotting the average number of segmented air clusters, N_{ave} , ver-
 202 sus the threshold values for experiments FFH and FFV, T_{FFH} and T_{FFV} , reveals distinct
 203 minima for these curves. The respective optimal threshold, T^* for these two experiments
 204 were $T_{\text{FFH}}^*=0.083$ and $T_{\text{FFV}}^*=0.105$. We selected a global value of $T^* = 0.094 \pm 0.014$
 205 (average from the two experiments $\pm 15\%$) Figure 2d) as the optimal threshold. Figure
 206 2e and f show the results of binarizing using the upper and lower bounds for T^* ($T_{\text{lb}}^* =$
 207 0.08 and $T_{\text{ub}}^* = 0.108$) and demonstrate that the most significant discrepancies occur where
 208 thin tendrils of water (black phase) connect two larger regions of water. We consider the
 209 range of possible interface locations as a source of uncertainty in calculations of satu-
 210 ration presented in Section 4. For Experiment MFH, the optimal threshold was $T_{\text{MFH}}^* =$
 211 0.042 ± 0.006 (Figure S3).

212 4 Experimental results

213 Images acquired during each experiment allow us to quantify the evolving phase
 214 distribution within the fracture. Figure 3 compares the primary and secondary drainage
 215 and imbibition cycles for horizontal experiments in the FF and MF fractures. The col-
 216 ors reflect air occupancy at sequential values of Ψ during each step of the experiment,
 217 with warm colors indicating smaller Ψ and cool colors indicating larger Ψ ; black regions
 218 remained water-filled for all Ψ . The grey regions in the secondary drainage figures are
 219 regions that remained air-filled at the end of primary imbibition.

220 [Figure 3 about here.]

221 For both experiments, air entered the fracture only after Ψ exceeded the air en-
 222 try pressure of the fracture ($\Psi_{\text{a,e}}$). Initial air entry occurred after the step from $\Psi = 274$
 223 mm to 325 mm for FFH and after the step from $\Psi = 174$ mm to 190 mm for MFH. The
 224 different values of $\Psi_{\text{a,e}}$ reflect differences in the fracture aperture along the two flow bound-
 225 aries for the two experiments. Though the nonporous glass surface and porous matrix
 226 were placed in contact to create the fractures, the size of the sintered beads used to cre-
 227 ate MF were larger than those used for FF (Figure S4), resulting in a larger aperture
 228 and lower $\Psi_{\text{a,e}}$ for MF. The Laplace-Young relationship relates $\Psi_{\text{a,e}}$ to the correspond-
 229 ing fracture apertures (see supporting information Text SS4 and Figure S5 for details)
 230 and suggests that the apertures along the flow boundaries are between 43 and 50 μm for
 231 FF and between 71 and 77 μm for MF.

232 The binarized distributions of air and water within the fracture at each increment
 233 of Ψ (Figure 3) allow us to quantify the areal fraction of the fracture occupied by wa-
 234 ter, S_w^A . This serves as a surrogate for volumetric water saturation, which we cannot pre-
 235 cisely quantify because we have only estimates of the fracture aperture and not aperture
 236 variability within the fracture. Figures 4a and 4b show Ψ plotted against S_w^A for each
 237 cycle of Experiments FFH and MFH, respectively. The Ψ versus S_w^A plots exhibit sig-
 238 nificant hysteresis, which can be understood by comparing the phase distributions dur-
 239 ing different cycles of each experiment.

240 [Figure 4 about here.]

241 As primary drainage proceeded through sequential steps of Ψ , air entered regions
 242 of progressively smaller aperture. For both FFH and MFH, the air first filled regions near
 243 the air-filled flow manifolds and then advanced through the center of the fracture un-
 244 til it connected the two manifolds. Then, with further decreases in Ψ , the region occu-
 245 pied by air expanded towards the no-flow boundaries. The similarity in the large-scale
 246 displacement pattern in both experiments likely reflects the influence of the clamping
 247 pressure applied to the aluminum frames during fracture assembly (Section 2), which leads
 248 to smaller apertures around the perimeter of the fracture. The small-scale features of
 249 the displacement patterns differ for the two experiments, likely due to the difference in
 250 the porous matrix, which influences the magnitude and variability of fracture aperture
 251 and matrix permeability.

252 A common feature of both experiments is the relative absence of regions of trapped
 253 water within the drained region of the fractures (i.e., isolated black regions surrounded
 254 by colored regions in Figure 3). This differs from experimental observations in fractures
 255 bounded by non-porous, impermeable surfaces, where regions of the draining phase be-
 256 come disconnected from the fracture edges and entrapped within the fracture (e.g., De-
 257 twiler et al., 2002; Chen et al., 2017). Here, water regions that become isolated during
 258 drainage eventually drain through the porous matrix if the aperture is large enough that
 259 Ψ exceeds the local air entry pressure in the fracture.

260 During primary imbibition, water fills the smallest aperture regions along the no-
 261 flow edges of the fractures first and then gradually advances towards the center of the
 262 fracture with each increment of Ψ . After water filled the fracture along the two flow man-

263 ifolds, the remaining air became entrapped and immobilized (dark red regions in second
 264 row from top in Figure 3). In contrast to the drainage process, the trapping observed
 265 during imbibition is similar to that observed in fractures bounded by non-porous, im-
 266 permeable surfaces. As a result, potentially large regions of air may become entrapped
 267 regardless of the presence of secondary porosity in the bounding porous matrix.

268 During secondary drainage (DR2) in FFH, air spreads more readily through the
 269 fracture than during DR1 due to the regions of trapped air remaining after IMB1. The
 270 result is that similar distributions of air and water within the fracture occur at lower val-
 271 ues of Ψ during DR2 than DR1. This can be observed in Figure 3 where the distribu-
 272 tions of air-filled regions at $\Psi=398$ mm in DR1 is similar to $\Psi=374$ mm in DR2. Like-
 273 wise the distribution of air-filled regions at $\Psi=423$ mm in DR1 is similar to $\Psi=398$ mm
 274 in DR2. Note, this history dependence is not observed for the imbibition cycles, where
 275 the initial distribution of air within the fracture was almost identical for IMB1 and IMB2,
 276 resulting in a nearly identical filling order (Figure 3). Similar behavior was observed in
 277 MFH, but because the drainage process occurred over a narrower range of Ψ , the dif-
 278 ferences between DR1 and DR2 are less pronounced.

279 In addition to the smaller $\Psi_{a,e}$ during primary drainage for the horizontal exper-
 280 iment in Model MF (Experiment MFH, Figure 4), another significant difference between
 281 FFH and MFH was the distribution of the air and water phases during each sequence.
 282 Specifically, the air clusters in MFH are more compact with less roughness of the air-
 283 water interfaces. Previous scaling analyses of two-phase displacements in fractures be-
 284 tween non-porous matrices suggest a reasonable explanation for this behavior (Glass et
 285 al., 1998, 2003). The competition between interfacial curvature in the fracture plane and
 286 across the fracture aperture have been shown to control the geometry of the air-water
 287 interfaces; smaller fracture apertures with more aperture variability lead to more tor-
 288 tuous interfaces than larger aperture fractures with less aperture variability.

289 Glass et al. (2003) derived the dimensionless parameter, $C/\delta = \frac{\langle b \rangle^2}{\sigma_b \lambda_b}$, where C is
 290 the dimensionless curvature number, a ratio of in-plane to out-of-plane interfacial cur-
 291 vature, δ is the coefficient of variation of the fracture aperture, and $\langle b \rangle$, σ_b , and λ_b are
 292 the mean, standard deviation, and correlation length of the aperture field. They showed
 293 that small C/δ led to tortuous air-water interfaces and as C/δ became larger entrapped
 294 regions of air became more compact. Though we cannot directly quantify C/δ for our

295 experiments, the air-entry apertures provide an estimate of $\langle b \rangle$. Because the aperture
 296 variability in our fractures are induced by the pore-scale variations of the porous sur-
 297 face, both σ_b and λ_b likely scale with the respective pore sizes of the porous plates. Be-
 298 cause the maximum pore sizes for MF are approximately 4 times larger than those in
 299 FF, this suggests that C/δ is an order of magnitude larger for MF than for FF. This likely
 300 explains the difference in the structure of the air-water interfaces for the two experimen-
 301 tal sequences.

302 It is not possible to directly measure the relative permeability of the air and wa-
 303 ter phases during our experiments, but we can estimate these values through numeri-
 304 cal simulations in the measured air-water distributions. For these simulations, we con-
 305 sidered only the influence of the geometry of the air and water on estimated relative per-
 306 meabilities. Detwiler et al. (2005) showed that the role of aperture variability on esti-
 307 mates of fracture relative permeability were minor relative to the distribution of the flow-
 308 ing phases within the fracture. We used the local cubic law to simulate flow of both air
 309 and water through the fracture for each value of Ψ represented in Experiments FFH and
 310 MFH. Figures 4c and 4d show the relationship between the estimated water and air rel-
 311 ative permeabilities, $k_{r,w}$ and $k_{r,a}$, respectively, and the areal saturation S_w^A of the wa-
 312 ter phase.

313 The relative permeability curves (Figures 4c and 4d) are qualitatively similar to
 314 what has been measured in both porous and fractured media in other studies, suggest-
 315 ing the potential utility of empirical permeability-saturation relationships for modeling
 316 flow through fractured porous media. However, the potential for the development of fracture-
 317 spanning regions of either air or water can strongly influence the evolution of $k_{r,w}$. This
 318 is most notable in comparing $k_{r,w}$ during primary and secondary drainage for FFH and
 319 MFH. The large region of air that forms at the entrance to FFH (Figure 3) caused a sig-
 320 nificant decrease in $k_{r,w}$ once $\Psi_{a,e}$ was exceeded. Conversely, in MFH, the more com-
 321 pact shape of the evolving air region led to a more gradual decrease in $k_{r,w}$.

322 5 Concluding Remarks

323 We have presented the development and evaluation of a new experimental system
 324 for exploring two-phase flow processes in porous fractured media. Use of light transmis-
 325 sion through the translucent porous fracture surface allows us to quantitatively delin-

326 eate the distribution of the evolving air-water interface within the fracture. Example ex-
327 periments in two different fractures demonstrated the role of changing pore pressure in
328 the porous matrix on the distribution of air and water within the fracture, which exhib-
329 ited significant hysteresis from the primary drainage through subsequent drainage cy-
330 cles

331 The primary advantage of this method over other approaches (e.g., 2D micromod-
332 els with a channel bounded by a porous matrix or X-ray CT in rock cores) is the abil-
333 ity to resolve the distribution of air and water within a fractured porous medium at: (i)
334 spatial scales that are much larger than the scale of aperture variability and the result-
335 ing regions of entrapped phases during displacement processes; and (ii) temporal scales
336 with the potential to resolve potentially rapidly evolving interfacial dynamics. In addi-
337 tion, the demonstration experiments presented here used a smooth glass plate as the up-
338 per fracture surface, but such experiments can be readily extended to include a rough
339 upper fracture surface to explore the relative importance of fracture-matrix interactions
340 and two-phase flow processes within a bounding variable aperture fracture.

341 **6 Open Research**

342 All experimental data and processing algorithms required to reproduce the results
343 presented here are publicly available (Liao et al., 2023).

344 **Acknowledgments**

345 The first author was supported by the scholarship under the State Scholarship Fund
346 from the China Scholarship Council for his visit to University of California, Irvine (CSC
347 student number: 201906270102). We also gratefully acknowledge the financial support
348 from the the Basic Science Center Program for Multiphase Media Evolution in Hyper-
349 gravity of the National Natural Science Foundation of China (No. 51988101), and the
350 National Natural Science Foundation of China (No. 51925906).

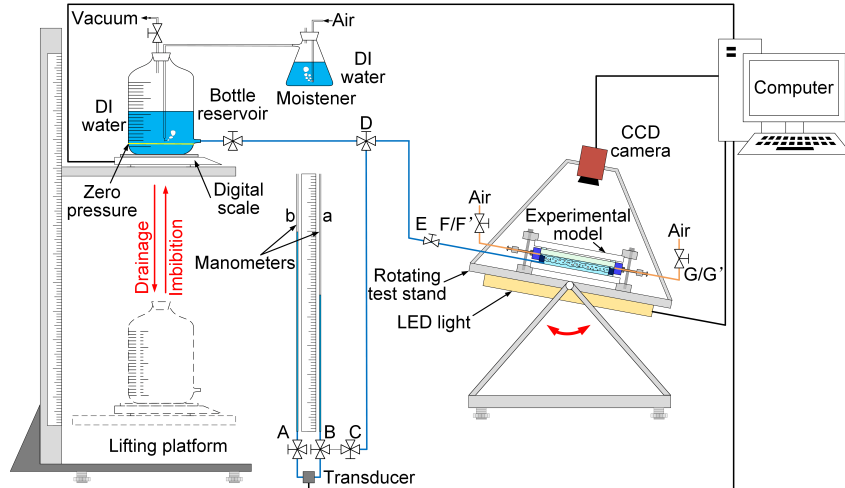
References

- 351
- 352 Arshadi, M., Khishvand, M., Aghaei, A., Piri, M., & Al-Muntasheri, G. A.
 353 (2018). Pore-scale experimental investigation of two-phase flow through
 354 fractured porous media. *Water Resources Research*, *54*(5), 3602-3631. doi:
 355 <https://doi.org/10.1029/2018WR022540>
- 356 Bitter, R., Mohiuddin, T., & Nawrocki, M. (2006). *Labview: Advanced programming*
 357 *techniques*. CRC Press.
- 358 Chen, Y., Fang, S., Wu, D., & Hu, R. (2017). Visualizing and quantifying the
 359 crossover from capillary fingering to viscous fingering in a rough fracture.
 360 *Water Resources Research*, *53*(9), 7756-7772.
- 361 Dearden, R., Noy, D., Lelliott, M., Wilson, R., & Wealthall, G. (2013, oct). Re-
 362 lease of contaminants from a heterogeneously fractured low permeability unit
 363 underlying a DNAPL source zone. *Journal of Contaminant Hydrology*, *153*,
 364 141–155. doi: 10.1016/j.jconhyd.2011.05.006
- 365 Detwiler, R. L., Pringle, S. E., & Glass, R. J. (1999). Measurement of frac-
 366 ture aperture fields using transmitted light: An evaluation of measurement
 367 errors and their influence on simulations of flow and transport through
 368 a single fracture. *Water Resources Research*, *35*(9), 2605-2617. doi:
 369 <https://doi.org/10.1029/1999WR900164>
- 370 Detwiler, R. L., Rajaram, H., & Glass, R. J. (2002). Experimental and simulated
 371 solute transport in a partially-saturated, variable-aperture fracture. *Geo-*
 372 *physical Research Letters*, *29*(8), 113–1–113–4. doi: [https://doi.org/10.1029/](https://doi.org/10.1029/2001GL013508)
 373 [2001GL013508](https://doi.org/10.1029/2001GL013508)
- 374 Detwiler, R. L., Rajaram, H., & Glass, R. J. (2005). Satiated relative permeability
 375 of variable-aperture fractures. *Physical Review E*, *71*, 031114. doi: [https://doi](https://doi.org/10.1103/PhysRevE.71.031114)
 376 [.org/10.1103/PhysRevE.71.031114](https://doi.org/10.1103/PhysRevE.71.031114)
- 377 Glass, R. J., Nicholl, M. J., & Yarrington, L. (1998). A modified invasion perco-
 378 lation model for low-capillary number immiscible displacements in horizontal
 379 rough-walled fractures: Influence of local in-plane curvature. *Water Resources*
 380 *Research*, *34*(12), 3215-3234. doi: <https://doi.org/10.1029/98WR02224>
- 381 Glass, R. J., Rajaram, H., & Detwiler, R. L. (2003). Immiscible displacements in
 382 rough-walled fractures: Competition between roughening by random aperture
 383 variations and smoothing by in-plane curvature. *Physical Review E*, *68*(6),

- 384 061110. doi: <https://doi.org/10.1103/PhysRevE.68.061110>
- 385 Haghighi, M., Xu, B., & Yortsos, Y. C. (1994). Visualization and simula-
386 tion of immiscible displacement in fractured systems using micromodels: I.
387 Drainage. *Journal of Colloid and Interface Science*, *166*(1), 168-179. doi:
388 <https://doi.org/10.1006/jcis.1994.1283>
- 389 Karpyn, Z. T., Halleck, P. M., & Grader, A. S. (2009). An experimental study of
390 spontaneous imbibition in fractured sandstone with contrasting sedimentary
391 layers. *Journal of Petroleum Science and Engineering*, *67*(1), 48-56. doi:
392 <https://doi.org/10.1016/j.petrol.2009.02.014>
- 393 Liao, Z., Detwiler, R. L., Cookson, E. S., Lei, W., & Chen, Y. (2023). *Dataset*
394 *for: Quantitative visualization of two-phase flow in a fracture porous medium*
395 [dataset]. doi: 10.5281/zenodo.8188007
- 396 Nicholl, M. J., Glass, R. J., & Wheatcraft, S. W. (1994). Gravity-driven infiltration
397 instability in initially dry nonhorizontal fractures. *Water Resources Research*,
398 *30*(9), 2533-2546. doi: <https://doi.org/10.1029/94WR00164>
- 399 Nicholl, M. J., Rajaram, H., Glass, R. J., & Detwiler, R. (1999). Saturated
400 flow in a single fracture: evaluation of the reynolds equation in measured
401 aperture fields. *Water Resources Research*, *35*(11), 3361-3373. doi:
402 <https://doi.org/10.1029/1999WR900241>
- 403 Persoff, P., & Pruess, K. (1995). Two-phase flow visualization and relative perme-
404 ability measurement in natural rough-walled rock fractures. *Water Resources*
405 *Research*, *31*(5), 1175-1186. doi: <https://doi.org/10.1029/95WR00171>
- 406 Rangel-German, E. R., & Kovscek, A. R. (2002). Experimental and analytical
407 study of multidimensional imbibition in fractured porous media. *Journal*
408 *of Petroleum Science and Engineering*, *36*(1), 45-60. doi: [https://doi.org/](https://doi.org/10.1016/S0920-4105(02)00250-4)
409 [10.1016/S0920-4105\(02\)00250-4](https://doi.org/10.1016/S0920-4105(02)00250-4)
- 410 Rangel-German, E. R., & Kovscek, A. R. (2006). A micromodel investigation of two-
411 phase matrix-fracture transfer mechanisms [Journal Article]. *Water Resources*
412 *Research*, *42*(3). Retrieved from <https://doi.org/10.1029/2004WR003918>
413 (<https://doi.org/10.1029/2004WR003918>) doi: [https://doi.org/10.1029/](https://doi.org/10.1029/2004WR003918)
414 [2004WR003918](https://doi.org/10.1029/2004WR003918)
- 415 Su, G. W., Geller, J. T., Pruess, K., & Wen, F. (1999). Experimental studies of
416 water seepage and intermittent flow in unsaturated, rough-walled fractures.

- 417 *Water Resources Research*, 35(4), 1019-1037. doi: <https://doi.org/10.1029/>
418 1998WR900127
- 419 Vafaie, A., Cama, J., Soler, J. M., Kivi, I. R., & Vilarrasa, V. (2023, may). Chemo-
420 hydro-mechanical effects of CO2 injection on reservoir and seal rocks: A review
421 on laboratory experiments. *Renewable and Sustainable Energy Reviews*, 178,
422 113270. doi: 10.1016/j.rser.2023.113270
- 423 Wan, J., Tokunaga, T. K., Orr, T. R., O'Neill, J., & Connors, R. W. (2000). Glass
424 casts of rock fracture surfaces: A new tool for studying flow and transport.
425 *Water Resources Research*, 36(1), 355-360. doi: <https://doi.org/10.1029/>
426 1999WR900289
- 427 Wan, J., Tokunaga, T. K., Tsang, C.-F., & Bodvarsson, G. S. (1996). Im-
428 proved glass micromodel methods for studies of flow and transport in frac-
429 tured porous media. *Water Resources Research*, 32(7), 1955-1964. doi:
430 <https://doi.org/10.1029/96WR00755>
- 431 Xu, B., Yortsos, Y. C., & Salin, D. (1998). Invasion percolation with viscous
432 forces. *Physical Review E*, 57, 739-751. doi: <https://doi.org/10.1103/>
433 PhysRevE.57.739
- 434 Yang, Z., Niemi, A., Fagerlund, F., & Illangasekare, T. (2012). A generalized ap-
435 proach for estimation of in-plane curvature in invasion percolation models
436 for drainage in fractures. *Water Resources Research*, 48(9), W09507. doi:
437 <https://doi.org/10.1029/2012WR011829>

(a) Experimental setup



(b) Experimental model

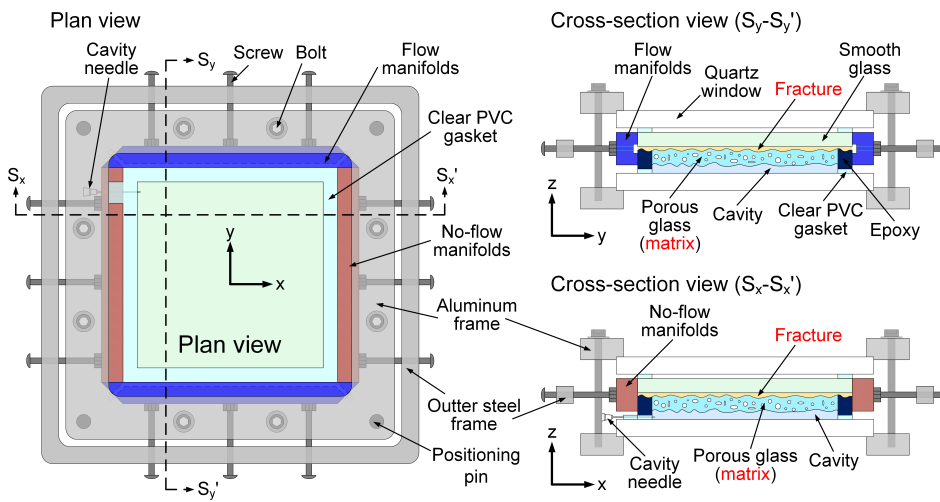


Figure 1. Schematic of experimental system including: (a) an overview of the experimental setup and (b) a plan view and cross-sections of the fracture test cell.

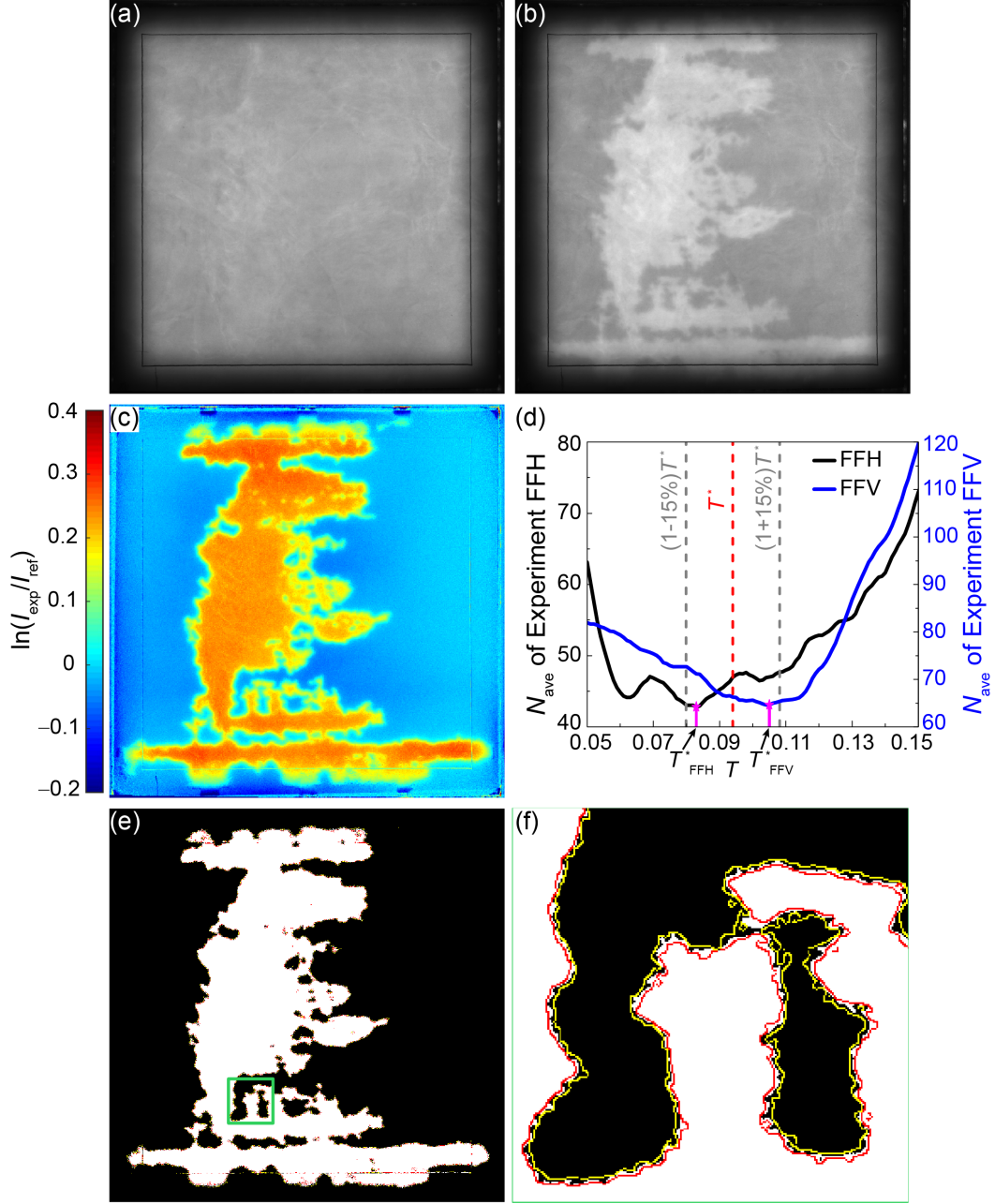


Figure 2. Overview of the image processing procedure, including: (a) The raw grayscale reference image, I_{ref} ; (b) an example of a raw grayscale experimental image, I_{exp} ; (c) the corresponding light absorbance field, $A = \ln(I_{\text{exp}}/I_{\text{ref}})$; (d) the relationship between the average number of segmented air clusters, N_{ave} , and the segmenting threshold values for Experiments FFH and FFV, T_{FFH} and T_{FFV} , revealing distinct minima for these curves; (e) the resulting binary image (black - water, white - air) determined using the global threshold with results using the upper and lower bounds of the global threshold indicated by yellow and red lines, respectively; (f) enlarged view of region indicated by the green box in (e).

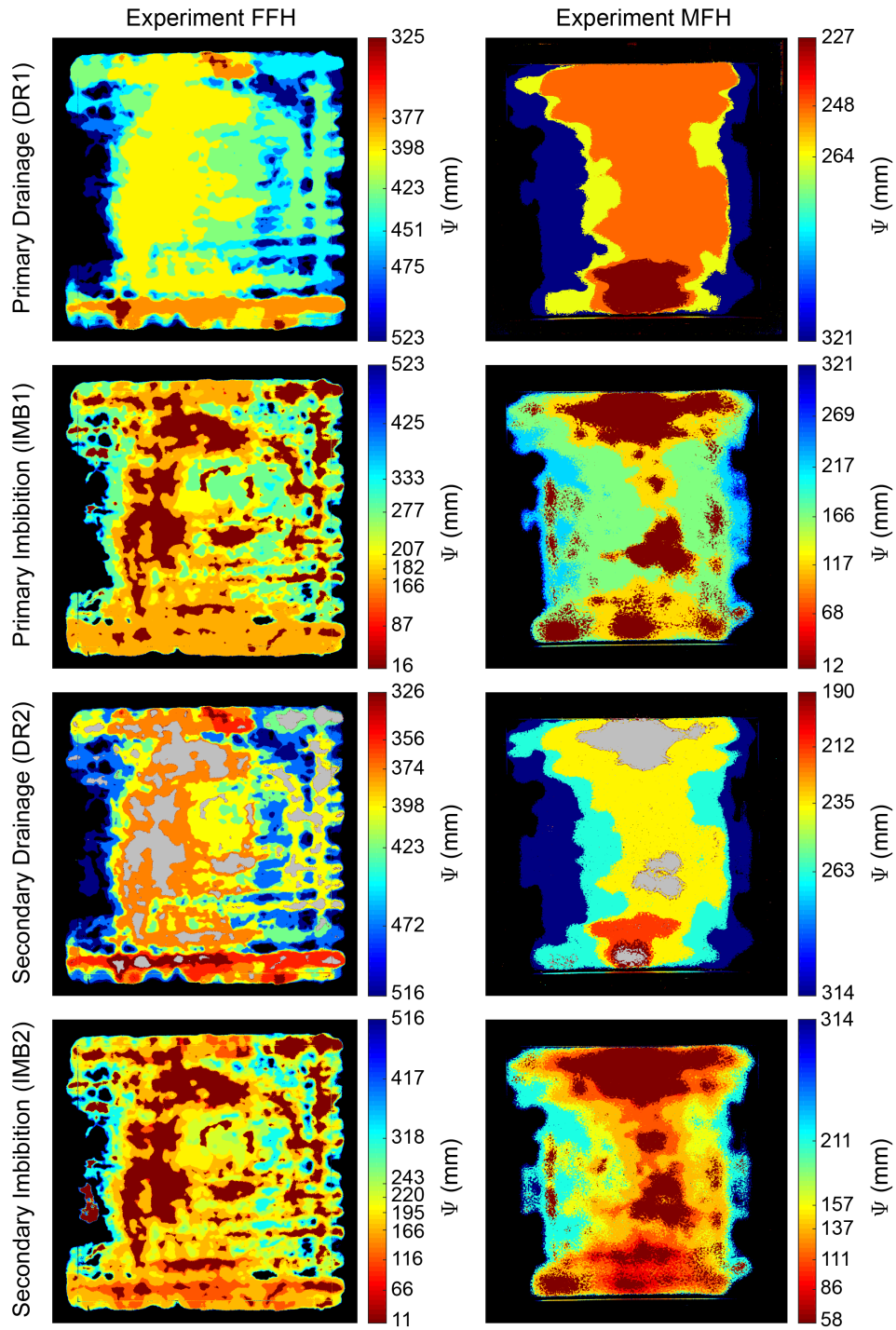


Figure 3. Phase evolution during cyclic drainage and imbibition processes of Experiments FFH and MFH. The average value of the applied capillary head, Ψ , is used to represent each pressure step. Discrete Ψ steps are indicated by the numbers next to the color bar for each sequence and the sequences proceed from top to bottom of each color bar. Warm colors are smaller values of Ψ and cool colors are larger values of Ψ . The color bar range for each drainage cycle begins at the first indication of air entry into the fracture.

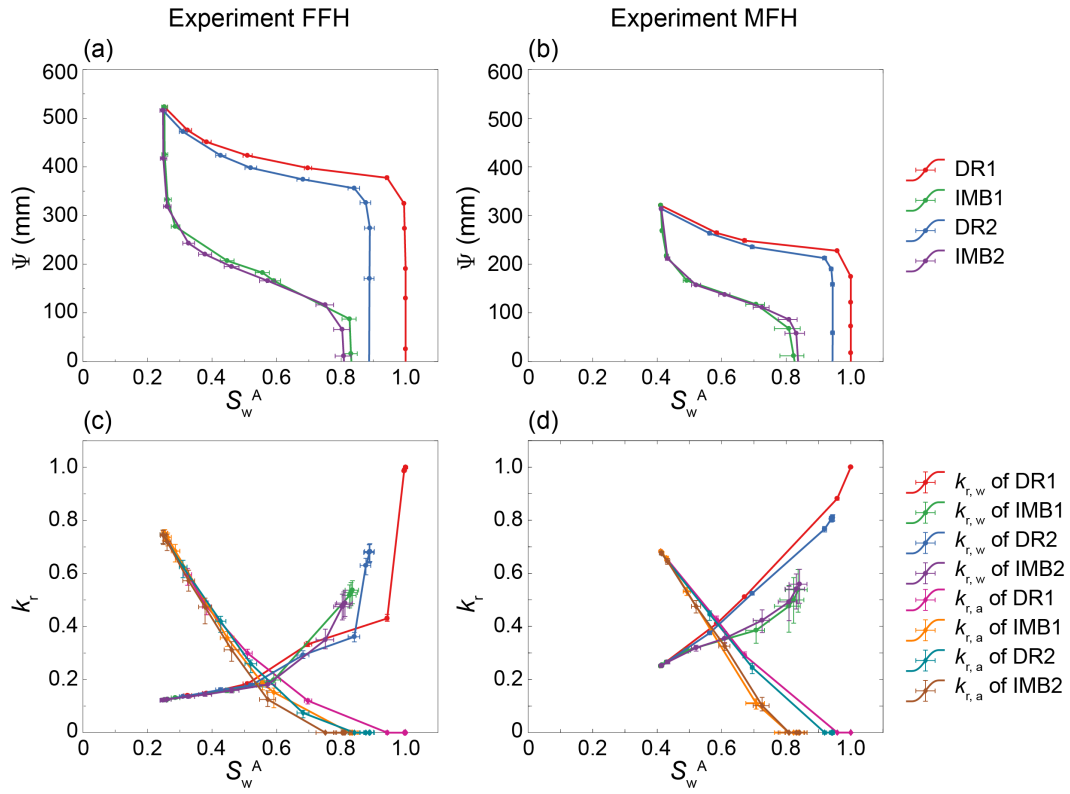


Figure 4. Relationship between applied capillary head Ψ and areal water saturation S_w^A for Experiment FFH (a) and MFH (b), and relationship between modeled relative permeability of water or air ($k_{r,w}$, $k_{r,a}$) and areal water saturation S_w^A for Experiment FFH (c) and MFH (d), in which S_w^A , $k_{r,w}$ and $k_{r,a}$ are the average values during the last 1 min in each step.